

# Atom Interferometric Imaging of Differential Potentials Using an Atom Laser

M. E. Mossman,<sup>1,2</sup> Ryan A. Corbin,<sup>2</sup> Michael McNeil Forbes,<sup>2,\*</sup> and P. Engels<sup>3,†</sup>

<sup>1</sup>*Department of Physics and Biophysics, University of San Diego, San Diego, California 92110, USA*

<sup>2</sup>*Department of Physics and Astronomy, Washington State University, Pullman Washington 99164, USA*

<sup>3</sup>*Department of Physics and Astronomy, Washington State University, Pullman Washington 99164 USA*

Interferometry is a prime technique for modern precision measurements. Atoms, unlike light, have significant interactions with electric, magnetic, and gravitational fields, making their use in interferometric applications particularly versatile. Here, we demonstrate atom interferometry to image optical and magnetic potential landscapes over an area exceeding  $240\ \mu\text{m} \times 600\ \mu\text{m}$ . The differential potentials employed in our experiments generate phase imprints in an atom laser that are made visible through a Ramsey pulse sequence. We further demonstrate how advanced pulse sequences can enhance desired imaging features, e.g. to image steep potential gradients. A theoretical discussion is presented that provides a semiclassical analysis and matching numerics.

**Introduction** — From optical precision measurements [1] to detecting minute ripples in space-time [2], interferometry is a keystone of modern science. Compared to their light-based counterparts, matter-wave interferometers have some decisive advantages [3], including significant sensitivity to electric, magnetic, and gravitational fields [4–6]. Access to both motional and internal degrees of freedom makes atom interferometers suitable for many applications, including timekeeping with ultracold atoms [7], inertial measurements [8, 9], and fundamental studies of quantum dynamics [10–13].

Here, we demonstrate the two-dimensional imaging of differential potentials based on atom interferometry with an atom laser – a coherent stream of atoms. Atom lasers [14–29] can be generated by coherently outcoupling atoms from a trapped dilute-gas Bose-Einstein condensate (BEC) into an untrapped quantum state, creating a two-dimensional sheet of atoms in an accelerated reference frame. Our interferometric imaging technique employs a Ramsey pulse sequence [30, 31]: two sequential  $\pi/2$  pulses, via coherent microwaves, separated by a wait time. The resulting images reveal contourlike lines of an applied differential potential. The potential causes a phase imprint that can be measured across the entire atom laser in a single run of the experiment, extending over an area exceeding  $240\ \mu\text{m} \times 600\ \mu\text{m}$ . Unlike previous atom interferometric work with a pulsed-output atom laser [32] or with thermal atoms [33], our work utilizes a quasicontinuous atom laser to map out two-dimensional potential landscapes. We demonstrate this technique with two types of differential potentials: a magnetic field that acts differently on two hyperfine states due to the Zeeman effect, and an optical dipole potential that is tuned to be attractive for one hyperfine state and repulsive for another.

As a practical application, we image a magnetic quadrupole field present in our experimental chamber, and show how a variation of the imaging pulse sequence can enhance desired features. Experimental results are well described by a semiclassical theory. Future applications include material science studies in hybrid quantum systems [34], studies of interaction effects in quantum caustics [35–37], and branched flow [38].

**Experimental procedure and results** — Our experiments begin with a dilute-gas BEC of  $\sim 4 \times 10^6$  atoms of  $^{87}\text{Rb}$  in the  $|F, m_F\rangle = |1, -1\rangle$  hyperfine state. The BEC is held in a

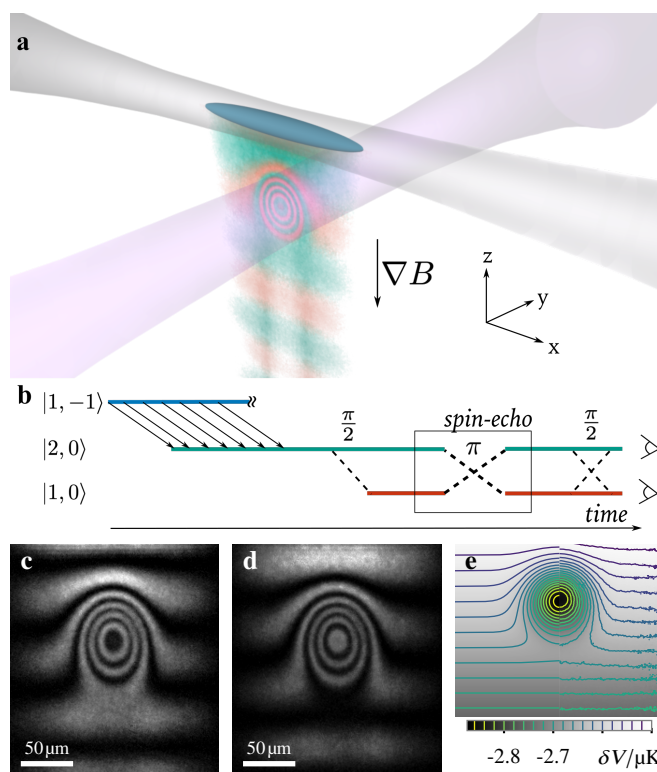


**Figure 1.** **a)** Experimental setup: a BEC (blue) of  $^{87}\text{Rb}$  atoms in the  $|F, m_F\rangle = |1, -1\rangle$  state is held in a dipole trap (gray). Atoms transferred to the  $|2, 0\rangle$  state are accelerated out of the trap in the presence of gravity and a magnetic gradient, generating an atom laser that travels downward. An additional optical laser (violet) crosses the atom laser to generate weak differential potentials. **b)** Interferometric imaging procedure. A first Ramsey pulse places the whole extent of the atom laser into a superposition state. Optionally, a  $\pi$  pulse can be inserted for realizing a spin echo. After a wait time, a second Ramsey pulse closes the interferometer with an arbitrary controllable phase, e.g., **c)**  $\theta = 0$  and **d)**  $\theta = \pi$ . The images in **c)** and **d)** are taken with a Ramsey pulse spacing of 0.70 ms and have each been averaged over ten independent runs of the experiment. **e)** By directly fitting the interference patterns (left), or with phase retrieval techniques (right), we can accurately reconstruct the differential potential  $\delta V(x, z)$ . See [Supplementary Material](#) for details.

hybrid trap formed by a focused infrared laser that provides mostly radial confinement, and a quadrupole magnetic field that provides additional support against gravity and axial con-

finement [Fig. 1a]. The resulting harmonic trap frequencies are  $\{\omega_x, \omega_y, \omega_z\} = 2\pi \times \{3.7, 39.7, 30.1\}$  Hz, with the weakly confined  $x$  axis directed horizontally in the images. From this trapped BEC, a coherent stream of atoms is outcoupled to form an atom laser by using microwave radiation that gradually transfers atoms to the  $|2, 0\rangle$  state, which is only weakly supported by the magnetic gradient. These transferred atoms fall out of the trap, accelerating downward from the injection site. After 10 ms of continuous outcoupling from the BEC, a brief 68  $\mu\text{s}$ -long microwave pulse puts the entire atom laser into a coherent superposition of the  $|2, 0\rangle$  and  $|1, 0\rangle$  state.

The falling atoms can be further manipulated with a dipole potential created by impinging focused laser light that is detuned from a resonant transition. Under appropriate conditions, this can lead to strong mechanical effects such as intricate patterns of caustics [29]. The sign and strength of the dipole potential depend on the intensity and wavelength of the laser in relation to the resonance lines of the atom. Here, we exploit this versatility by choosing a laser wavelength such that the resulting potential is attractive for atoms in the  $|1, 0\rangle$  state and repulsive for atoms in the  $|2, 0\rangle$  state. See [Supplementary Material](#) for more details. The dipole potential focuses or defocuses the  $|1, 0\rangle$  or  $|2, 0\rangle$  atom lasers respectively, and can in both cases form caustics for sufficiently high powers [29]. Here we use weak dipole strengths that have only small mechanical effects on the atom laser, probing mostly the so-called ‘‘Aharonov-Bohm’’ phase [6]. The dipole is centered  $z_d = 89.9(4)$   $\mu\text{m}$  below the injection site, and the Gaussian waist radius of the dipole laser  $w = 38.9(6)$   $\mu\text{m}$  is smaller than the transverse extent of the atom laser ( $\approx 240$   $\mu\text{m}$ ).

In addition to the dipole potential, a differential potential for atoms in the  $|1, 0\rangle$  and  $|2, 0\rangle$  states can be generated by a magnetic field, shifting their energies by the quadratic Zeeman effect. Here, with a background field of approximately 10 G and a vertical gradient of  $dB/dz = -25.10(1)$  G/cm, the energy of the  $|2, 0\rangle$  ( $|1, 0\rangle$ ) state increases (decreases) with  $h \times 12.43(6)$  kHz/mm in the  $-z$  direction, determined using a linear approximation across the region of magnetic fields covered by the atom laser (see [Supplementary Material](#) for details). This magnetic field is present in the full region of the atom laser, whereas the dipole laser is focused to a region just below the trapped position of the BEC.

Atom interferometric imaging is performed by a Ramsey pulse sequence [Fig. 1b] followed directly by absorption imaging along the  $-y$  direction with a 10  $\mu\text{s}$ -long imaging pulse. The first 68  $\mu\text{s}$ -long microwave  $\pi/2$  pulse mentioned above creates a coherent superposition of the outcoupled  $|1, 0\rangle$  and  $|2, 0\rangle$  states. After an evolution time  $t_{\text{wait}}$ , a second 68  $\mu\text{s}$ -long Ramsey pulse is applied to close the interferometer and apply an arbitrary phase shift. Because of the large hyperfine splitting of the  $^{87}\text{Rb}$  ground state, atoms are imaged spin selectively.

In the presence of a differential potential, the phase evolution between the two Ramsey pulses leads to interference patterns observed in the spin-selective images. In [Figs. 1c to 1d](#) and [Fig. 2](#), this potential consists of the magnetic gradient along the vertical direction and [except in [Fig. 2a](#)] the dipole

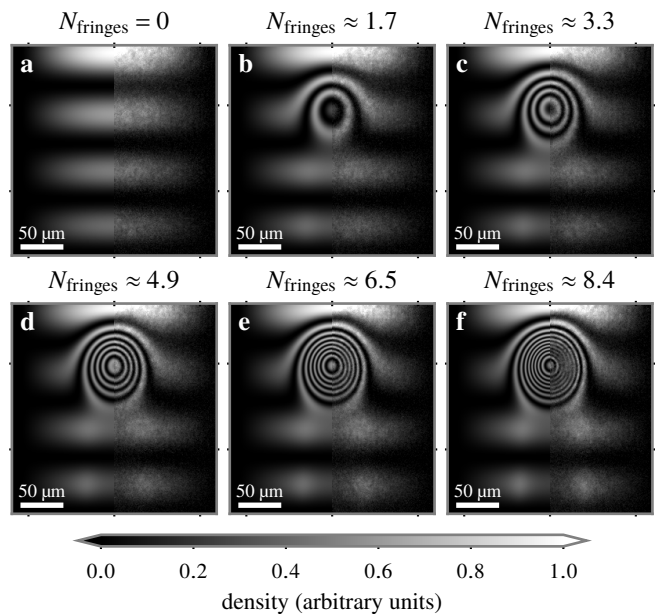


**Figure 2.** Atom interferometric imaging of a combined magnetic and optical differential potential for several powers of the dipole potential. Each frame is split vertically and shows the theory result (left) compared to the experimental image (right). The experimental images were taken with a Ramsey pulse spacing of 0.5 ms and are averages of 30 experimental runs. The images show the atoms in the  $|2, 0\rangle$  state. The energy differences generated by the dipole beam between the  $|2, 0\rangle$  and  $|1, 0\rangle$  are (a) 0  $\mu\text{K}$ , (b) 0.16(7)  $\mu\text{K}$ , (c) 0.32(6)  $\mu\text{K}$ , (d) 0.47(4)  $\mu\text{K}$ , (e) 0.6(2)  $\mu\text{K}$ , and (f) 0.81(7)  $\mu\text{K}$ , and are obtained with uncertainties by least-squares fitting of the experimental data with our model as described in [Supplementary Material](#). Each title shows the expected number of fringes created by the dipole potential [Eq. (7)] estimated using the impulse approximation.

potential intersecting the atom laser. The differential potential was constant throughout the experiment, but switched off just before imaging. The magnetic potential leads to the observation of horizontal interference stripes [Fig. 2a], while the dipole potential causes the bull’s-eye pattern seen in the upper part of the atom laser. For short pulse sequences, these approximate contour lines of the differential potential [see Eq. (7)]. Phase retrieval [39–41] or direct fitting techniques can be used to extract the potential shape, as demonstrated in [Fig. 1e](#).

In [Fig. 2](#), the depth of the dipole potential is increased from panel to panel, increasing the number of interference rings in the bull’s-eye pattern commensurate with the increased phase accumulation between the two Ramsey pulses. Matching numerics, shown in the left side of each panel in the figure, are in excellent agreement with the experimental images. Because of the low dipole laser intensities used in [Fig. 2](#), the mechanical effects on the atom laser are small in the sense that no pronounced caustics are formed. For the  $|2, 0\rangle$  state imaged in [Fig. 2](#), the dipole potential is weakly repulsive, leading to a small but increasing suppression of the density in the region below the dipole laser as the power is increased.

*Semiclassical analysis and quantitative comparison with experiment* — To theoretically treat our system, we approximate

the physics using a semiclassical analysis [28, 42, 43]. To start, consider a system uniform along  $x$ , which is a good approximation near the center of our laser. Atoms are injected into the system at rest from the trapped cloud at height  $z = z_0$  and are immediately subject to a time-dependent potential  $V(z, t)$  that includes both gravity and any external potentials, causing the atoms to fall. Atoms are continuously injected into the system, so atoms imaged at time  $t_i$  and height  $z_i$  will have been injected at some earlier time  $t_0(t_i, z_i) \leq t_i$ , which must be determined by solving the classical boundary-value problem:

$$m\ddot{z}(t) = -\frac{\partial}{\partial z}V(z(t), t), \quad (1a)$$

$$z(t_0) = z_0, \quad \dot{z}(t_0) = 0, \quad z(t_i) = z_i. \quad (1b)$$

We capture the effects of the various state transitions in the form of the potential  $V(z, t)$ : if a particle initially in the  $|2, 0\rangle$  state is subject to Ramsey pulse transition  $|2, 0\rangle \rightarrow (|2, 0\rangle + |1, 0\rangle)/\sqrt{2}$  at time  $t_1$ , then we must track two different classical trajectories, having the same potential  $V(z, t)$  for  $t < t_1$ , but different species-dependent potentials  $V_i(z, t)$  for later times.

In our analysis, we further assume  $V(z_0, t) = 0$  for all times, such that the classical Hamiltonian at the injection site  $H_0 = 0$ , capturing the essence of coherence in the atom laser: injection occurs resonantly at a fixed energy, keeping the phase of the injected particles constant over time  $\psi_0(z_0, t) = \psi_0(z_0)$ .

The wave function follows from the path integral:

$$\psi(z, t) = \int dz_0 \int \mathcal{D}[q] \exp\left\{\frac{i}{\hbar}S[q]\right\} \psi(z_0, t_0), \quad (2a)$$

$$S[q] = \int_{t_0}^t dt \left( \frac{m\dot{q}^2}{2} - V(q(t), t) \right). \quad (2b)$$

where the integral is taken over all paths  $q(t)$  subject to the boundary conditions  $q(t) = z$  and  $q(t_0) = z_0$ , and  $S[q]$  is the classical action. We assume highly localized injection  $\psi(z_0, t_0) \propto \delta(z_0)$ , which we take to be about  $z_0 = 0$ . (See [Supplementary Material](#) for details.)

The Wentzel-Kramers-Brillouin (WKB) approximation amounts to expanding the action

$$S[q + \xi] = S[q] + S'[q] \cdot \xi + \frac{1}{2!}S''[q] \cdot \xi\xi + \dots \quad (3)$$

about the classical trajectories  $q_{cl}$  where  $S'[q_{cl}] = 0$ . Keeping only the quadratic fluctuations [42] with  $S[q_{cl}] \equiv S(z, t; z_0, t_0)$ ,

$$\psi_{\text{WKB}}(z, t) = \int dz_0 \sqrt{\frac{-\partial^2 S / (2\pi i \hbar)}{\partial z \partial z_0}} e^{iS/\hbar} \psi(z_0, t_0). \quad (4)$$

If there are multiple trajectories that arrive at the same final position  $z(t_i)$  at the time of imaging, one must add these amplitudes to obtain the appropriate interference pattern.

For this position-to-position transition,

$$\frac{\partial S}{\partial z} = p(t), \quad \frac{\partial S}{\partial z_0} = -p(t_0), \quad \text{and} \quad \frac{\partial^2 S}{\partial z \partial z_0} = \frac{\partial p}{\partial z_0}. \quad (5)$$

If the force is conservative,  $E = p^2/2m + V(z) = p_0^2/2m + V(z_0)$  and one recovers the familiar factor of  $\sqrt{p}$  in the denominator of  $\psi_{\text{WKB}}(z, t)$ :

$$p(z_0, t_0) = -\sqrt{p_0^2 + 2m(V(z_0) - V(z))}, \quad \frac{\partial p}{\partial z_0} \propto \frac{1}{p}. \quad (6)$$

The semiclassical problem is thus reduced to solving for the classical trajectories of particles injected at  $q(t_0) = (x_0, z_0)$  that end up at  $q(t_i) = (x, z) \equiv \vec{x}$  in the image.

When preparing numerical simulations for the experiment, we interfere two different trajectories: those of the particles which remain in state  $|2, 0\rangle$  ( $\psi_1$ ) and those which start in the state  $|2, 0\rangle$  but are converted to state  $|1, 0\rangle$  for times between the two Ramsey pulses ( $\psi_2$ ). This procedure has a few deficiencies. First, the semiclassical amplitudes diverge at the turning point  $z = z_0$ . This can be remedied by using Airy functions, but to demonstrate the accuracy of the pure semiclassical calculation, we simply exclude the region close to the injection site in our comparisons. Second, the model assumes instantaneous state transitions. We mitigate this by allowing the transition to occur at a time slightly shifted from the middle of the transition window that accounts for the acceleration of the particles. A proper semiclassical accounting for this effect requires a multicomponent WKB approximation [44–47], which is much more complicated and not needed here.

The interference pattern  $I_n \propto |\psi_1 + \psi_2|^2$  can be modeled as  $I_n(\vec{x}) \approx a(\vec{x}) + b(\vec{x}) \cos(\phi(\vec{x}) + \theta_n)$  where  $\theta_n$  is an experimentally controllable phase. Phase retrieval techniques [39–41] can efficiently extract the difference in actions between the paths  $\hbar\phi(\vec{x}) = S_1(\vec{x}) - S_2(\vec{x}) + \text{const.}$ , from which the differential potential can be extracted. This requires imaging at least three different values of  $\theta_n$  (see [Supplementary Material](#)).

Alternatively, if the form of the potential is known up to a few parameters, then the interference pattern can be directly modeled from a single value of  $\theta_n$ , allowing high-precision fitting of these parameters. This analysis is the basis for our numerical simulations and leads to a quantitative explanation of the experimental data, as demonstrated in [Fig. 2](#). With a few simplifying approximations that we call the ‘‘impulse approximation’’ – assuming weak potentials do not appreciably deflect the particles, and the transitions and  $t_{\text{wait}}$  are sufficiently fast such that the particles do not fall significantly during the Ramsey pulse sequence – one obtains the following density pattern, and corresponding expected number of maxima (fringes) in the interference pattern:

$$n_{2,0}^{\text{Ramsey}} \propto 1 - \cos\left(\frac{t_{\text{wait}}}{\hbar} \delta V\right), \quad N_{\text{fringes}} \approx \frac{t_{\text{wait}} \delta V_{\text{max}}}{2\pi\hbar}, \quad (7)$$

where  $\delta V_{\text{max}}$  is the maximum of the differential potential  $\delta V(\vec{x})$ , (see also [Supplementary Material](#)). This agrees well with the full calculations and experiments, as shown in [Fig. 2](#).

*Magnetic field mapping* — So far, we have demonstrated the effect of combined magnetic and optical differential potentials using Ramsey pulse sequences between the  $|2, 0\rangle$  and  $|1, 0\rangle$  states. This transition is only weakly sensitive to magnetic fields



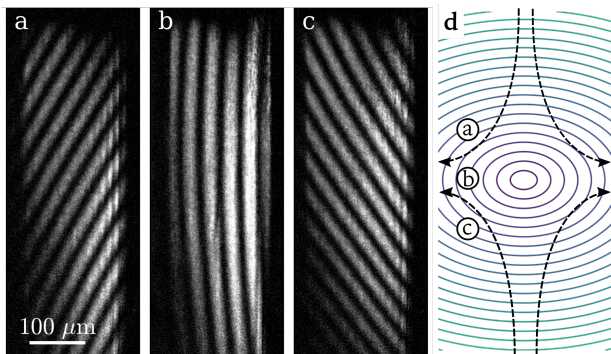


**Figure 3.** Atom interferometric fringe pattern using the magnetically sensitive transition between  $|1, -1\rangle$  and  $|2, -2\rangle$ . A magnetic quadrupole field with gradient  $dB/dz = 140(10)$  mG/cm was placed with its center to the right and **a**) slightly below, **b**) right next to, and **c**) slightly above the atom laser. The Ramsey pulses are spaced by 2 ms. The images show the atoms detected in the  $|2, -2\rangle$  state after the Ramsey sequence. Each image is from a single repetition of the experiment. **d**) Schematic representation of quadrupole field (not to scale). Letters correspond to panels **a**) to **c**) and indicate the position of quadrupole field. The magnetic gradient has been calculated from the interference pattern in panel **b**).

due to second order Zeeman effects. In applications where a greater sensitivity to magnetic fields is desired, a strongly magnetic field dependent transition such as the one between the stretched states  $|1, -1\rangle$  and  $|2, -2\rangle$  can be employed. In  $^{87}\text{Rb}$ , this transition shifts by  $-2.1$  MHz/G in low fields, compared to 11 kHz/G for the  $|1, 0\rangle$  to  $|2, 0\rangle$  transition in a bias field of 10 G. When using magnetically sensitive transitions, care must be taken that the Ramsey pulses affect the entire atom laser, otherwise a state transfer will occur in only a small region, which can be used for fluid flow tracing [29].

We demonstrate the capability of using the  $|1, -1\rangle$  to  $|2, -2\rangle$  transition to detect small magnetic gradient fields in Fig. 3. Here, an atom laser is generated from a BEC confined in a purely optical trap: a large-diameter dipole beam is employed to provide mostly radial confinement, and two repulsive, thin dipole sheets are added as “end caps” on the left and right side of the BEC to provide axial confinement. The atom laser is then realized by ramping down the intensity of the large-diameter dipole beam to create a wide atom laser without relying on any preexisting magnetic gradient for the output coupling. To generate a test pattern, a magnetic quadrupole field with an axial gradient of  $140(10)$  mG/cm was added, approximately 2 orders of magnitude smaller than the gradient used for the previous images. The position of the quadrupole field zero was adjusted relative to the imaging window using small magnetic bias fields, as shown schematically in Fig. 3d. The results clearly show the tilt of the equipotential lines in the magnetic quadrupole field, demonstrating the capability of imaging magnetic field gradients in a single experimental run.

*Spin-echo imaging* — Atom interferometric techniques provide great flexibility for the design of experimental sequences. While the experiments described above have all used a Ramsey pulse sequence, extended sequences can be employed to en-

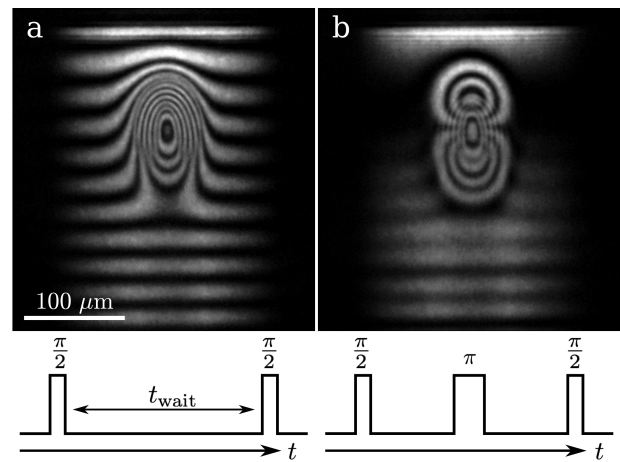


**Figure 4.** Comparison of (a) Ramsey imaging and (b) spin-echo imaging. Pulse sequence timelines are depicted below each image (not drawn to scale). Both images show the  $|2, 0\rangle$  state 0.5 ms after the end of the pulse sequence. Total wait time between the  $\pi/2$  pulses is  $t_{\text{wait}} = 1504 \mu\text{s}$  in both cases. Images have been averaged over 30 independent experimental runs of the same parameters.

hance specific features. One example is demonstrated in Fig. 4 where the Ramsey sequence has been augmented by inserting an additional  $\pi$  pulse, realizing a spin-echo sequence. Such a sequence can be used to cancel the effects of constant differential potentials and to produce contour lines of the gradient along the direction of motion. For Fig. 4a, a pulse spacing  $t_{\text{wait}}$  of  $1504 \mu\text{s}$  between the two pulses of a Ramsey sequence was used, with each  $\pi/2$  pulse lasting  $53 \mu\text{s}$  and connecting the  $|2, 0\rangle$  and  $|1, 0\rangle$  states. The corresponding spin-echo sequence shown in Fig. 4b was chosen to have the same total length of the sequence between the Ramsey pulses. The two panels in Fig. 4 show that, over a significant region in the upper part of the atom laser, the spin-echo sequence suppresses the horizontal stripes caused by the weak magnetic gradient, while imaging the gradient of the dipole potential along the vertical direction. The oval-shaped features in the center of Fig. 4b are a consequence of an inefficiency of the  $\pi$  pulse in the center of the potential where light shifts are significant. Similarly, the cancellation of the horizontal stripe pattern near the bottom of the image is incomplete as the  $\pi$  pulse is slightly shifted out of resonance here. In principle, these issues could be mitigated if sufficient microwave power is available by applying shorter pulses with larger linewidths. This demonstrates the capabilities of suitably chosen pulse sequences to enhance or modify the imaging contrast of desired features.

*Conclusion* — As demonstrated in this work, atom interferometric imaging with an atom laser is a powerful tool for detecting and evaluating differential potentials over a large two-dimensional area. With the availability of highly tunable pulse sequences and several accessible spin states for measuring a variety of differential potentials, this technique is highly versatile and can be adapted for a wide set of applications. As an applied example, relating to work presented in Ref. [34], one can consider applications to material science where a material under



study is placed parallel to the sheet of an atom laser, detecting the magnetic fields emanating from the material by imaging them in the plane of the atom laser using the interferometric technique.

P.E. acknowledges support from the [National Science Foundation \(NSF\)](#) through Grant No. [PHY-1912540](#) and from the [Ralph G. Yount Distinguished Professorship at Washington State University \(WSU\)](#). M.E.M. acknowledges support from the [NSF](#) through Grant No. [PHY-2137848](#) and from the [Clare Boothe Luce Professorship Program of the Henry Luce Foundation](#). R.A.C. and M.M.F. acknowledge support from the [NSF](#) through Grant No. [PHY-2012190](#).

## Supplementary Material

### Differential dipole potential

The differential dipole potential is generated with a laser locked to the  $F = 3$  to  $F' = 4$  transition of  $^{85}\text{Rb}$ . The light is  $\pi$ -polarized with respect to the bias field applied to the atoms. With laser powers on the order of a hundred nW sent to the atoms and a Gaussian beam waist of  $39\ \mu\text{m}$ , differential potential depths of few hundreds of nK are generated at the atom laser sheet. Potential depths can be theoretically estimated, for example by following Ref. [48].

### Output Ports

Fig. 5 shows the two complementary output ports of the interferometer, imaging the  $|1, 0\rangle$  or  $|2, 0\rangle$  states after the Ramsey sequence, respectively. This provides an alternative way to obtain the information shown in Figs. 1c to 1d for two phase shifts separated by a  $\pi$  phase shift.

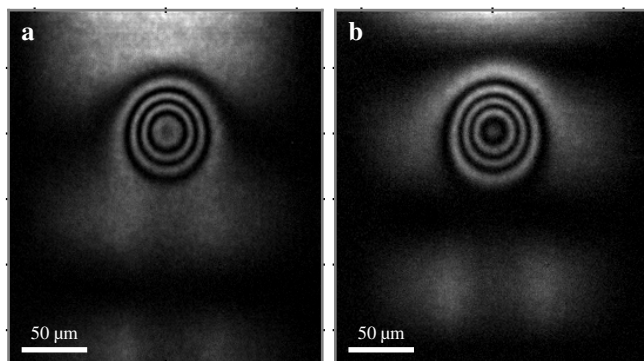


**Figure 5.** The a)  $|1, 0\rangle$  and b)  $|2, 0\rangle$  states form two complementary output ports of the interferometer that can separately be imaged. The images shown here are taken with a Ramsey pulse spacing of 0.25 ms. Each image has been averaged over 30 runs of the experiment. As the imaging transition is stronger for the  $|2, 0\rangle$  state, the intensities of the two panels have been independently scaled.

### Influence of Ramsey time

The observed spacing between the interference fringes is a function of the differential phase accumulation occurring between the two Ramsey pulses. This phase accumulation not only depends on the depth of the potential, but also on the chosen time between the two pulses. This dependence on the pulse spacing is demonstrated in Fig. 6, where a magnetic gradient of  $-25.1\ \text{G/cm}$  was used to generate a differential potential for the  $|2, 0\rangle$  and  $|1, 0\rangle$  state. Here, Figs. 6a to 6e were taken under identical conditions but for Ramsey pulse spacings of  $t_{\text{wait}} = \{0.1, 0.5, 1.5, 2.5, 5.0\}$  ms, respectively. The density of lines caused by the magnetic gradient increases with the pulse

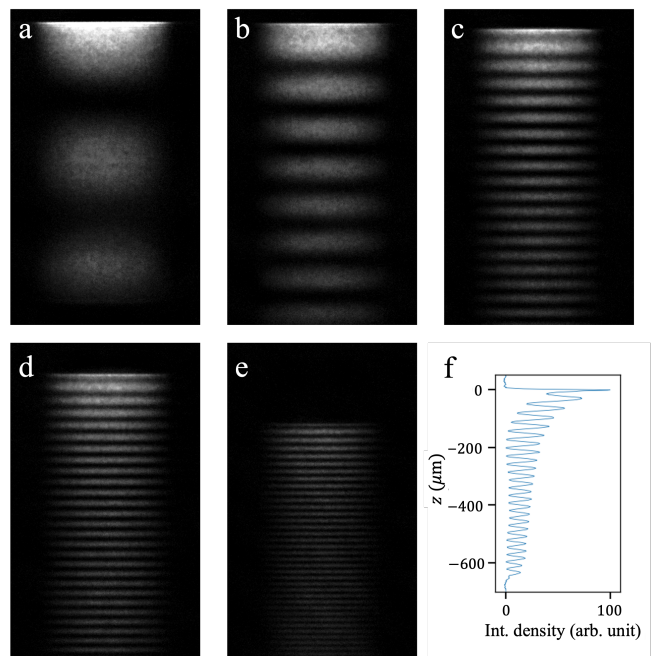


**Figure 6.** Atom interferometric fringe pattern as a function of Ramsey pulse spacing. Images are taken in the presence of a magnetic gradient; no dipole potential has been applied. The Ramsey pulse spacing is (a) 0.1 ms, (b) 0.5 ms, (c) 1.5 ms, (d) 2.5 ms, (e) 5 ms. Each of the two Ramsey pulses has a pulse length of 68  $\mu\text{s}$ . Panel (f) shows the horizontally integrated cross section of (c). All image intensities are scaled with the same factor for comparison. Each panel has been averaged over 10 independent runs with the same experimental parameters.

spacing as expected. Fig. 6f shows a horizontally integrated cross section of Fig. 6c.

### Determination of the magnetic gradient

To determine the magnetic gradient present for the data shown in Fig. 1, Fig. 2, Fig. 4 and Fig. 6, a spectroscopic technique is employed, where we use the highly magnetic sensitive transition between the  $|2, -2\rangle$  and  $|1, -1\rangle$  states. An atom laser is generated comprised of atoms in the  $|2, -2\rangle$  hyperfine state. Using a weak and brief microwave pulse with a duration of 50  $\mu\text{s}$ , a thin, horizontal stripe of atoms is transferred into the  $|1, -1\rangle$  state immediately before an image is taken. In contrast to the images shown in the main text where the Ramsey pulses transferred the whole atom laser, here a microwave pulse only transfers a small stripe of atoms. In images taken of the  $|2, -2\rangle$  atom laser, this stripe appears as a dark horizontal line as indicated by the white markers in Fig. 7. The position of this line is determined, and the corresponding magnetic field is calculated based on the applied microwave frequency and the Breit-Rabi formula. This procedure is repeated for a variety of microwave frequencies, resulting in a map of the magnetic field as a function of position.

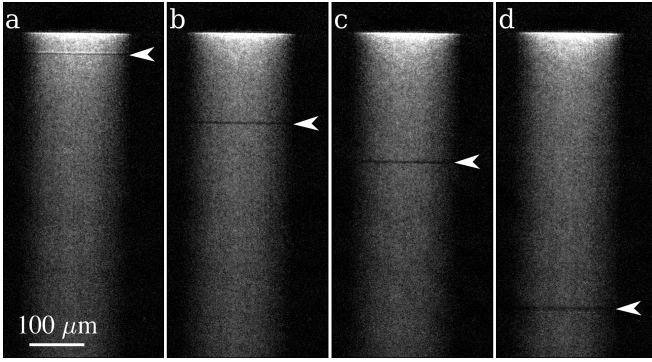


**Figure 7.** Spectroscopic mapping of magnetic field contour lines using fluid flow tracing. Microwave frequency **a** 6.8147 GHz, **b** 6.814 GHz, **c** 6.8136 GHz, and **d** 6.8121 GHz. The white markers indicate the position where atoms are transferred. The intensity for all images has been scaled identically for comparison. Each panel is the result of a single run of the experiment.

### Fitting the Data

Simulations are fit to the experimental data by varying important system parameters and numerically minimizing an overlap function that yields a measure of  $\chi_r^2$  for the simulation. We identify as meaningful the following parameters:

- $V_0$ : The potential depth generated by the Gaussian beam, proportional to the laser power. A higher power leads to more interference fringes in the optical region, and to more pronounced shadows below the beam. In a typical experiment, one controls the power of the laser, hence  $V_0$  depends on both the power and the waist of the optical beam: a wider beam distributes the power over a large area, reducing  $V_0$ . Thus, for our simulations, we use  $V_0$  which directly correlates with the number of fringes according to Eq. (7) if the impulse approximation is valid.
- $w$ : The waist of the optical beam. A larger waist shifts the apparent center of the potential down slightly.
- $z_0$ : The location of the center of the optical beam in the  $z$  direction, relative to the atom laser injection site. This is a convenience parameter for aligning the simulations to the experimental data and does not affect the major physical features.
- $t_{\text{wait}}$ : The time between Ramsey pulses entirely dictates the horizontal interference pattern in the atom laser. The wait time also affects the number of interference fringes within the region of the optical laser, with longer wait times leading to more interference fringes (see Eq. (7)).
- $R_{\text{ab}}$ : The relative potential depths for particles occupying the  $|2, 0\rangle$  and  $|1, 0\rangle$  states.
- $V_{\text{dev}}$ : This is a linear piece in the form of the optical potential, modelling a deviation in the potential from a pure Gaussian. This affects the optical fringes by making the

beam more powerful, and also slightly shifts the apparent location of the center of the beam. This parameter is intended to model a tiny but visible asymmetry in the fringe pattern above and below the center of the beam.

- $\lambda_i$ : an offset for the time at which the particles begin to feel the  $\pi/2$  pulse. This parameter is implemented in order to simulate that particles in the atom laser do not instantly feel the effects of the  $\pi/2$  pulse, but will on average feel it at the center of its pulse time. This is well approximated by a value of  $\lambda_i = 0.5$ .

	$V_0$ [ $\mu\text{K}$ ]	$z_0$ [ $\mu\text{m}$ ]	$w$ [ $\mu\text{m}$ ]	$R_{\text{ab}}$	$V_{\text{dev}}$	$\chi_r^2$
b)	0.16(7)	89.7(9)	39(2)	3(5)	-0.00(9)	3.0
c)	0.32(6)	90.0(7)	39(1)	1(2)	0.00(4)	2.8
d)	0.47(4)	90.0(7)	39.0(8)	1(1)	0.00(2)	3.7
e)	0.6(2)	90(1)	38.9(7)	1(1)	-0.00(7)	5.3
f)	0.81(7)	90.0(5)	39.1(6)	0.7(7)	0.00(2)	9.2

**Table I.** Best fit parameter values for our model for each of the data-sets in Figs. 2b to 2f. (Fig. 2a has no information about the differential-dipole potential, so we do not fit it.) The error estimates are the  $1\sigma$  deviations based on a standard minimization of the reduced  $\chi_r^2$  (Eq. (8)), scaling the final results so that  $\chi_r^2 = 1$ . The fits include  $73\,700 = 268 \times 275$  pixels for  $|x| < 120\,\mu\text{m}$  and  $z \in [-275\,\mu\text{m}, -30\,\mu\text{m}]$ . This excludes the original cloud and any systematic deviations from neglecting the Airy functions in our semiclassical calculation as well as any effects from non-uniform fields below the injection site.

The horizontal striping effect is purely due to the Ramsey pulse spacing  $t_{\text{wait}}$ , while the fringes in the vicinity of the dipole potential are due to both  $t_{\text{wait}}$  and  $V_0$ .

We perform a least-squares minimization over these parameters of

$$\chi_r^2 = \frac{1}{\nu} \sum \frac{(n_{\text{theory}} - n_{\text{experiment}})^2}{(\sigma n_{\text{max}})^2} \quad (8)$$

where we estimate  $\sigma \approx 0.00056$  as the standard deviation of the background thermal fluctuations taken from a dark patch of the image, scaled by the normalization factor applied to the data before minimization. The sum is over  $73\,700 = 268 \times 275$  pixels for  $|x| < 120\,\mu\text{m}$  and  $z \in [-275\,\mu\text{m}, -30\,\mu\text{m}]$ . Fitting 5 parameters gives  $\nu = 73\,694$  degrees of freedom.

The final  $\chi_r^2$  values listed in Table I indicate that the fits are not consistent with this thermal noise. The residuals shown in Fig. 8 give some hints about deficiencies of the model. A large residual in the troughs of the interference fringes are likely due to several effects include:

- Using a single injection point. A more accurate model would convolve the results over the full injection region, reducing the purity of the interference between the states.
- Each experimental image is an average of  $\sim 30$  shots. The clarity of the interference patterns demonstrates the repeatability of experiment, but one expects slight variations in environmental conditions between images that could shift parameters like  $z_d$  slightly from run to run,



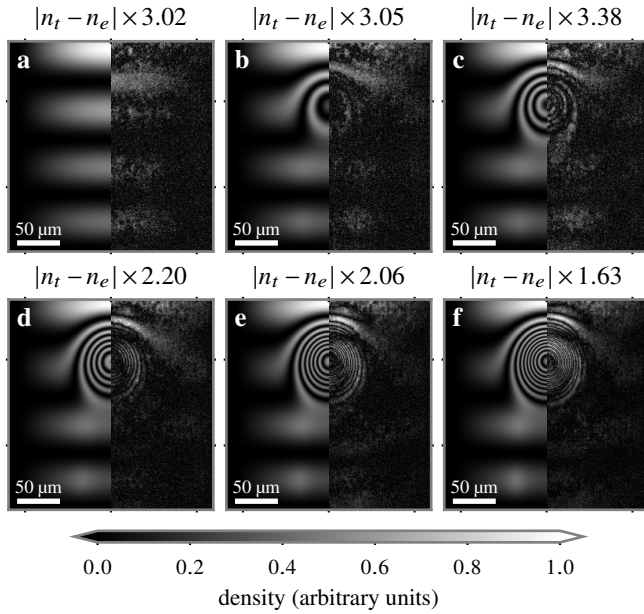


**Figure 8.** Residuals of the best fit semiclassical model with the experimental data. The frames correspond to those in Fig. 2. Each frame is split vertically and shows the theory result  $n_t \equiv n_t^{\text{theory}}$  (left) compared to the scaled residuals (right). The residuals are scaled so that the maximum residual matches the maximum theory density to facilitate comparison. These scaling factors are listed in the title of each frame.

smearing the experimental images most noticeably in the dark regions. One might mitigate this by individually fitting each shot.

- Our model assumes perfectly Gaussian beams. There are likely deviations beyond what we tried to model through  $V_{\text{dev}}$  and  $R_{\text{ab}}$  due to optics and 3D geometry. An interesting future direction is to try to perform parameter-free reconstructions of the potential from the interference patterns, but for accuracy, using a well-defined form is always preferable.

### Coherence of the Atom Laser

As a check of our semi-classical analysis, we model a pure atom laser in a constant gravitational field through the two-component Hamiltonian (see also [28, 49–51] for similar analysis):

$$i\hbar \frac{\partial}{\partial t} |\Psi\rangle = \hat{H} |\Psi\rangle, \quad |\Psi(t)\rangle = \begin{pmatrix} |\psi_a(t)\rangle \\ |\psi_b(t)\rangle \end{pmatrix},$$

$$\hat{H} = \begin{pmatrix} \frac{\hat{p}_z^2}{2m} + mg\hat{z} & \Omega e^{i\omega t} \\ \Omega e^{-i\omega t} & \frac{\hat{p}_z^2}{2m} + V(\hat{z}) \end{pmatrix}.$$

The idea of an atom laser is that a large reservoir of the lower component is held in the trapping potential  $V(z)$ . The off-diagonal coupling converts this lower component  $|\psi_b\rangle$  to the

upper component  $|\psi_a\rangle$ ,<sup>1</sup> which then falls in the gravitational field. If the off-diagonal coupling is small, then one can treat the trapped component as a constant, and we have the following coupled equation (essentially neglecting the lower-left block):

$$i\hbar |\dot{\psi}_a(t)\rangle = \left( \frac{\hat{p}_z^2}{2m} + mg\hat{z} \right) |\psi_a(t)\rangle + \Omega e^{i\omega t} |\psi_b(t)\rangle$$

$$i\hbar |\dot{\psi}_b(t)\rangle = \left( \frac{\hat{p}_z^2}{2m} + V(\hat{z}) - E_b \right) |\psi_b(t)\rangle.$$

After some time, the states become quasi-stationary, and we can write:

$$|\psi_b(t)\rangle = |\psi_b\rangle e^{-iE_b t/\hbar}, \quad |\psi_a(t)\rangle = |\psi_a\rangle e^{i(\hbar\omega - E_b)t/\hbar},$$

$$\left( \frac{\hat{p}_z^2}{2m} + mg\hat{z} - i\hbar\partial_t \right) |\psi_a(t)\rangle = -\Omega e^{i(\hbar\omega - E_b)t/\hbar} |\psi_b\rangle,$$

$$\left( \frac{\hat{p}_z^2}{2m} + V(\hat{z}) - E_b \right) |\psi_b\rangle = 0,$$

$$\left( \frac{\hat{p}_z^2}{2m} + mg\hat{z} + \hbar\omega - E_b \right) |\psi_a\rangle = -\Omega |\psi_b\rangle,$$

$$\left( \frac{\hat{p}_z^2}{2m} + mg(\hat{z} + z_0) \right) |\psi_a\rangle = -\Omega |\psi_b\rangle.$$

The last equation is simplified by setting  $mgz_0 = \hbar\omega - E_b$ , which we can redefine as the zero of our coordinate system  $z \rightarrow z - z_0$ . Doing this, and rescaling  $\tilde{z} = z/\xi$ , we have:

$$\left( -\frac{\partial^2}{\partial \tilde{z}^2} + \tilde{z} \right) \psi_a(\tilde{z}) = -\frac{2m\Omega\xi^2}{\hbar^2} \psi_b(\tilde{z}), \quad \xi = \sqrt[3]{\frac{\hbar^2}{2m^2g}}.$$

The homogeneous solution can be expressed in terms of the Airy functions:

$$\psi(\tilde{z}) = a \text{Ai}(\tilde{z}) + b \text{Bi}(\tilde{z}),$$

where  $y = \text{Ai}(\tilde{z})$  and  $y = \text{Bi}(\tilde{z})$  are the orthogonal real solutions with  $\lim_{\tilde{z} \rightarrow \infty} \text{Ai}(\tilde{z}) = 0$  to

$$y'' = \tilde{z}y,$$

and the full solution can be expressed in terms of the Green's function (see e.g. [52, 53])

$$G(\tilde{z}, \tilde{z}') = -\pi \begin{cases} \text{Ai}(\tilde{z}') \text{Ci}(\tilde{z}) & \tilde{z} \leq \tilde{z}', \\ \text{Ai}(\tilde{z}) \text{Ci}(\tilde{z}') & \tilde{z} \geq \tilde{z}' \end{cases},$$

$$\text{Ci}(\tilde{z}) = \text{Bi}(\tilde{z}) + i \text{Ai}(\tilde{z}),$$

$$\left( \frac{\partial^2}{\partial \tilde{z}^2} - \tilde{z} \right) G(\tilde{z}, \tilde{z}') = \delta(\tilde{z} - \tilde{z}'),$$

$$\psi_a(\tilde{z}) = \frac{2m\Omega\xi^2}{\hbar^2} \int d\tilde{z}' G(\tilde{z}, \tilde{z}') \psi_b(\tilde{z}').$$

<sup>1</sup> In our experiment  $|\psi_b\rangle$  corresponds to the hyperfine state  $|1, -1\rangle$ , while  $|\psi_a\rangle$  initially corresponds to the hyperfine state  $|2, 0\rangle$ . At time  $t \approx t_1$  the  $|2, 0\rangle$  state is mixed with the  $|1, 0\rangle$  hyperfine state, which would require a three-component formalism.

(The homogeneous contributions vanish if there are no obstructions below the injection site.) Note that the output is coherent [26] and has a smooth density dependence  $n_a(z) = |\psi_a(z)|^2 \propto 1/\sqrt{-z}$  as remarked in Fig. 1 of [54] and seen in [55] – there are no density oscillations of the type indicated in Fig. 3 of [56].

For  $z < 0$ , the qualitative form can be deduced from the WKB approximation:

$$\begin{aligned} \psi_{\text{WKB}}(z) &\propto \frac{1}{\sqrt{p(z)}} e^{S(z)/i\hbar}, \\ z(t) &= -\frac{gt^2}{2}, \quad p(z) = -mgt = -m\sqrt{-2gz} \\ S(z) &= \int_0^t \left( \frac{p^2}{2m} - mgz(t) \right) dt = \frac{-mg^2 t^3}{3} = -\hbar \frac{2}{3} \sqrt{\frac{-z^3}{g^3}}, \\ \psi_{\text{WKB}}(z) &\propto \frac{1}{|z|^{1/4}} \exp\left( \frac{2i}{3} \sqrt{\frac{-z^3}{g^3}} \right) \end{aligned}$$

### Interferometry

To qualitatively understand the interferometry of our setup, we make a few approximations. We first assume that the pulses are short so that we can effectively treat them as instantaneous.

*Ramsey Imaging* — Let the first  $\pi/2$  Ramsey pulse happen at time  $t_1$  and the second  $\pi/2$  Ramsey pulse at time  $t_2 = t_1 + t_{\text{wait}}$ . We then ignore the complication that different states take slightly different trajectories so that we can consider the particles as a single two-state system with the two falling states  $|2, 0\rangle$  and  $|1, 0\rangle$ .

Immediately prior to the pulse at  $t_1$ , the falling atoms are in state  $|\psi_{t_1^-}\rangle = |2, 0\rangle$  (we use the notation  $t_1^\pm = t_1 \pm \epsilon$  for small  $\epsilon$ ). After the first  $\pi/2$  pulse, the state is  $|\psi_{t_1^+}\rangle \propto |2, 0\rangle + |1, 0\rangle$  with suitably defined axes. The states now fall until  $t = t_2$  accumulating phases  $\theta_{2,0}^{12}$  and  $\theta_{1,0}^{12}$  respectively:  $|\psi_{t_2^-}\rangle \propto \exp(i\theta_{2,0}^{12})|2, 0\rangle + \exp(i\theta_{1,0}^{12})|1, 0\rangle$ . After the second  $\pi/2$  pulse, we have

$$\begin{aligned} |\psi_{t_2^+}\rangle &\propto e^{i\theta_{2,0}^{12}}(|2, 0\rangle + |1, 0\rangle) + e^{i\theta_{1,0}^{12}}(-|2, 0\rangle + |1, 0\rangle) \\ &\propto \left( e^{i\theta_{2,0}^{12}} - e^{i\theta_{1,0}^{12}} \right) |2, 0\rangle + \left( e^{i\theta_{2,0}^{12}} + e^{i\theta_{1,0}^{12}} \right) |1, 0\rangle. \end{aligned} \quad (9)$$

The two output channels thus give rise to the following interference patterns:

$$n_{2,0}^{\text{Ramsey}} \propto 1 - \cos(\theta_{2,0}^{12} - \theta_{1,0}^{12}), \quad (10a)$$

$$n_{1,0}^{\text{Ramsey}} \propto 1 + \cos(\theta_{2,0}^{12} - \theta_{1,0}^{12}). \quad (10b)$$

Using two-component notation with upper component  $|2, 0\rangle$  and lower component  $|1, 0\rangle$ , the  $\pi/2$  pulses (about the  $y$  axis) have matrix form

$$U_{\pi/2} = \frac{1}{\sqrt{2}} \begin{pmatrix} 1 & -1 \\ 1 & 1 \end{pmatrix}. \quad (11)$$

We can thus summarize the procedure as

$$\begin{pmatrix} 1 \\ 0 \end{pmatrix} \xrightarrow{\pi/2} \frac{1}{\sqrt{2}} \begin{pmatrix} 1 \\ 1 \end{pmatrix} \xrightarrow{\frac{\pi}{2}} \frac{1}{2} \begin{pmatrix} e^{i\theta_{2,0}^{12}} - e^{i\theta_{1,0}^{12}} \\ e^{i\theta_{2,0}^{12}} + e^{i\theta_{1,0}^{12}} \end{pmatrix}.$$

$t = t_1^- \quad t = t_1^+ \quad t = t_2^- \quad t = t_2^+$

*Spin-Echo Imaging* — We can use a similar notation to consider the spin-echo procedure with an additional  $\pi$ -pulse at time  $t_1 < t_e < t_2$ :

$$U_{\pi} = \begin{pmatrix} 0 & -1 \\ 1 & 0 \end{pmatrix}. \quad (12)$$

$$\begin{aligned} \begin{pmatrix} 1 \\ 0 \end{pmatrix} &\xrightarrow{\pi/2} \frac{1}{\sqrt{2}} \begin{pmatrix} 1 \\ 1 \end{pmatrix} \xrightarrow{\frac{\pi}{2}} \frac{1}{\sqrt{2}} \begin{pmatrix} e^{i\theta_{2,0}^{1e}} \\ e^{i\theta_{1,0}^{1e}} \end{pmatrix} \xrightarrow{\pi} \frac{1}{\sqrt{2}} \begin{pmatrix} -e^{i\theta_{1,0}^{1e}} \\ e^{i\theta_{2,0}^{1e}} \end{pmatrix} \xrightarrow{\frac{\pi}{2}} \frac{1}{2} \begin{pmatrix} -e^{i(\theta_{1,0}^{1e} + \theta_{2,0}^{e2})} - e^{i(\theta_{2,0}^{1e} + \theta_{1,0}^{e2})} \\ -e^{i(\theta_{1,0}^{1e} + \theta_{2,0}^{e2})} + e^{i(\theta_{2,0}^{1e} + \theta_{1,0}^{e2})} \end{pmatrix} \\ &t = t_1^- \quad t = t_1^+ \quad t = t_e^- \quad t = t_e^+ \\ &t = t_2^- \quad t = t_2^+ \end{aligned}$$

This gives the following interference patterns:

$$n_{2,0}^{\text{spin-echo}} \propto 1 + \cos\left( (\theta_{1,0}^{1e} + \theta_{2,0}^{e2}) - (\theta_{2,0}^{1e} + \theta_{1,0}^{e2}) \right), \quad (13a)$$

$$n_{1,0}^{\text{spin-echo}} \propto 1 - \cos\left( (\theta_{1,0}^{1e} + \theta_{2,0}^{e2}) - (\theta_{2,0}^{1e} + \theta_{1,0}^{e2}) \right). \quad (13b)$$

*Impulse Approximations* — To gain further insight, we make the approximation that the pulses and  $t_{\text{wait}}$  are short enough that the atoms fall a negligible amount while the potentials are imprinted. We call this the impulse approximation, because we can neglect the kinetic energy contribution to the action. Under this approximation, we accumulate the following phases:

$$\theta_a^{12} = \frac{S^{12}}{\hbar} \approx \frac{1}{\hbar} \int_{t_1}^{t_2} -V_a(z(t)) dt \approx \frac{t_1 - t_2}{\hbar} V_a\left(\frac{z_1 + z_2}{2}\right). \quad (14)$$

Thus, the interferometer Eq. (10) qualitatively measures the difference  $\delta V(z) = V_{2,0}(z) - V_{1,0}(z)$  between the two potentials:

$$n_{2,0}^{\text{Ramsey}} \propto 1 - \cos\left(\frac{t_{\text{wait}}}{\hbar} \delta V(z)\right) \quad (15)$$

where  $z$  is the location of the particles at  $t \approx t_1 \approx t_2$ . This allows us to define the following dimensionless quantity which roughly characterizes the number of maxima (fringes) expected in the interference pattern, as demonstrated in Fig. 2:

$$N_{\text{fringes}} = \frac{t_{\text{wait}} \delta V_{\text{max}}}{2\pi\hbar} \quad (16)$$

where  $\delta V_{\text{max}} = \max_z \delta V(z)$  is the maximum of the differential potential.

Relaxing the impulse approximation, the interference pattern will be smeared, stretched, and will fall as the particles continue

to accelerate downwards between the pulse sequences and the imaging time. In principle, this motion can be backed out to provide direct interferometric tomography of the potentials, but much higher accuracy can be obtained by directly fitting the potential.

If we consider the spin-echo imaging with  $t_e = (t_1 + t_2)/2$  in the middle, then Eq. (13) gives the following interference pattern:

$$\begin{aligned} n_{2,0}^{\text{spin-echo}} &\propto 1 + \cos\left(\frac{t_{\text{wait}}(\delta V(z_{1e}) - \delta V(z_{e2}))}{2\hbar}\right) \\ &\approx 1 + \cos\left(\frac{t_{\text{wait}}^2 \vec{p} \cdot \vec{\nabla} \delta V(z)}{4m\hbar}\right). \end{aligned} \quad (17)$$

Here  $z_{1e}$  and  $z_{e2}$  are approximately the midpoints between the  $\pi/2$  and  $\pi$  pulses, and are separated by time  $t_{\text{wait}}/2$ , giving a finite difference between the potentials that effectively differentiates the potential in the direction of propagation  $\vec{p}$ , again subject to the smearing, stretching, and falling as the impulse approximation is relaxed. This is clearly visible in the spin-echo imaging Fig. 4b where the gradient gives two lobes compared to the Ramsey imaging in Fig. 4a which outlines the potential difference itself.

Relaxing the requirement of weak potentials, the pre-factor in WKB approximation will become important, and the interference pattern will start to lose contrast. Additionally, shadows and transverse focusing will affect the amplitude of the final pattern: the full fitting process properly includes these effects far from the turning point, allowing for a more precise extraction of the potential parameters.

### Phase Retrieval

If the form of the potential is not available for accurate fitting as discussed above, one can provide direct interferometric tomography of the potential using phase retrieval techniques [39–41].

The essential idea is express the images  $I_n(\vec{x})$  in terms of the probability density

$$n_\theta(\vec{x}) = |\psi_1(\vec{x}) + e^{i\theta}\psi_2(\vec{x})|^2 \quad (18a)$$

where  $\psi_i(\vec{x})$  are the interfering wavefunctions in the WKB approximation,

$$\psi_i(\vec{x}) = A_i(\vec{x})e^{S_i(\vec{x})/i\hbar} \quad (18b)$$

and  $\theta$  is a relative phase that can be controlled experimentally. Since in our experimental implementation the interferometer is defined by two Ramsey pulses, phase shifting can be effected with very high precision by electronically varying the phase of the second Ramsey pulse.

By varying  $\theta$ , we obtain a set of images  $I_n \propto n_{\theta_n}$  with the

following form (excluding stochastic noise etc.):

$$\begin{aligned} I_n(\vec{x}) &\propto a(\vec{x}) + b(\vec{x}) \cos(\phi(\vec{x}) + \theta_n) \\ &= \underbrace{A_1^2(\vec{x}) + A_2^2(\vec{x})}_{a(\vec{x})} + \underbrace{A_1(\vec{x})A_2(\vec{x})}_{b(\vec{x})} \cos\left(\underbrace{\frac{S_2(\vec{x}) - S_1(\vec{x})}{i\hbar}}_{\phi(\vec{x})} + \theta_n\right). \end{aligned}$$

Expanding, we have

$$I_n(\vec{x}) \propto a(\vec{x}) + b(\vec{x}) \cos \phi(\vec{x}) \cos \theta_n - b(\vec{x}) \sin \phi(\vec{x}) \sin \theta_n,$$

thus, the set of images for different  $\theta_n$  form an ellipse in a three-dimensional sub-space of the space of images. Phase retrieval is straightforward, especially if  $\theta_n$  can be chosen at will as can be done in our experiment. Simply choose an equally spaced set of  $\theta_n = 2\pi n/N|_{n=0}^{N-1}$ . Averaging the images gives  $b(\vec{x})$ , allowing the phase  $\phi(\vec{x})$  to be retrieved:

$$b(\vec{x}) = \frac{1}{N} \sum_{n=0}^{N-1} I_n(\vec{x}), \quad \tan \phi(\vec{x}) = \frac{I_{\theta=0}(\vec{x}) - b(\vec{x})}{I_{\theta=-\pi/2}(\vec{x}) - b(\vec{x})}. \quad (19)$$

Reduction of stochastic errors can be achieved by using the singular-value decomposition (SVD) to extract the three principle components (eigenfaces) from the complete set of images.

The phase  $\phi(\vec{x})$  directly reconstructs the difference in action between the two trajectories, and the derivatives give access to the differential potential. To be explicit, for a conservative potential  $V(z)$  one has

$$\begin{aligned} S(z) &= Et - \int_{z_0}^z p(z) dz, \\ S'(z) &= -p(z) = \mp \sqrt{2m(E - V(z))}, \\ \hbar\phi'_1(z) - \hbar\phi'_2(z) &= \sqrt{2m(E - V_1(z))} - \sqrt{2m(E - V_2(z))}. \end{aligned}$$

Setting the energy  $E = 0$  at the injection site and expanding  $V_i(z) \approx V(z) \pm \delta(z)$  gives:

$$\delta(z) \approx \frac{\hbar\phi'_1(z) - \hbar\phi'_2(z)}{\sqrt{-2m/V(z)}}. \quad (20)$$

Fully inverting  $\delta S(x, z)$  for two-dimensional motion is more complicated, but for weak potential differences, everything can be done perturbatively with similar ease.

Our actual experiment is slightly more complicated due to the time-dependence, but the same analysis can be used for a slightly more complicated differential potential of the form

$$V(z) = \begin{cases} V_b(z) & z \in [z_1, z_2], \\ V_a(z) & \text{otherwise,} \end{cases} \quad (21)$$

where  $z_i = z(t_i)$  are the locations of the falling particles when the Ramsey pulses are applied. The complication is that these locations depend on the unknown differential potential  $\delta(z)$ , however, for weak potentials, these deviations are small, and the inverse problem can again be solved perturbatively. Note: this analyses does not assume the impulse approximation.



An analytic expression can be obtained if the differential potential is weak:

$$S(z_i) \approx S_0(z_i) - \int_{t_1}^{t_2} \delta V(z(t; z_i)) dt, \quad (22)$$

where  $z(t)$  is the classical trajectory of the particle that arrives at  $z = z(t_i, z_i)$  at the time of imaging. In this approximation, the contribution of  $S_0(z_i)$  will cancel from the interference pattern. Changing variables to the height  $z(t; z_f)$ , we have:

$$\delta S(z_i) = S_2(z_i) - S_1(z_i) \approx \int_{z_1(t_1; z_i)}^{z_2(t_2; z_i)} \frac{\delta V(z)}{\dot{z}(z)} dz, \quad (23)$$

where we note that, for weak potentials, the velocity  $\dot{z}$  depends only on  $z$ . Thus, the gradient of the interference pattern is

$$\delta S'(z_i) \approx \frac{\delta V(z)}{\dot{z}(z)} \frac{\partial z}{\partial z_i} \Big|_{z_1(t_1; z_i)}^{z_2(t_2; z_i)}. \quad (24a)$$

For a constant gravitational field  $V(z) = mgz$  and  $\dot{z} = -g(t - t_0) = -\sqrt{-2gz}$ , so

$$z(t; z_i) = -\frac{g}{2}(t - t_0(z_i))^2, \quad \frac{\partial z}{\partial z_i} = \frac{t - t_0(z_i)}{t_i - t_0(z_i)}, \quad (24b)$$

where we define  $\dot{z}_i = -\sqrt{-2gz_i}$  and

$$t_0(z_i) = t_i - \sqrt{\frac{-2z_i}{g}} = t_i + \frac{\dot{z}_i}{g}. \quad (24c)$$

Collecting everything:

$$\delta S'(z_i) \approx 2 \frac{\delta V(z_1(z_i)) - \delta V(z_2(z_i))}{\sqrt{-2gz_i}}. \quad (24d)$$

As a check, in the impulse approximation  $z_2 \approx z_1 + t_{\text{wait}} \dot{z}$ :

$$\delta S'(z_i) \approx \frac{\dot{z} t_{\text{wait}} \delta V'(\bar{z})}{\dot{z}_i}, \quad \bar{z} = \frac{z_1 + z_2}{2}. \quad (25a)$$

This is consistent with

$$\delta S(z_i) = t_{\text{wait}} \delta V(\bar{z}(z_i)) \quad (25b)$$

since

$$\frac{\partial \bar{z}}{\partial z_i} = \frac{\dot{z}}{\dot{z}_i}. \quad (25c)$$

As demonstrated in Fig. Fig. 9, the two methods of reconstructing the differential potential (either from direct experimental phase reconstruction methods or from fitting by matching data using the impulse approximation) result in nearly identical potential shapes and depths over a large area of the atom laser.

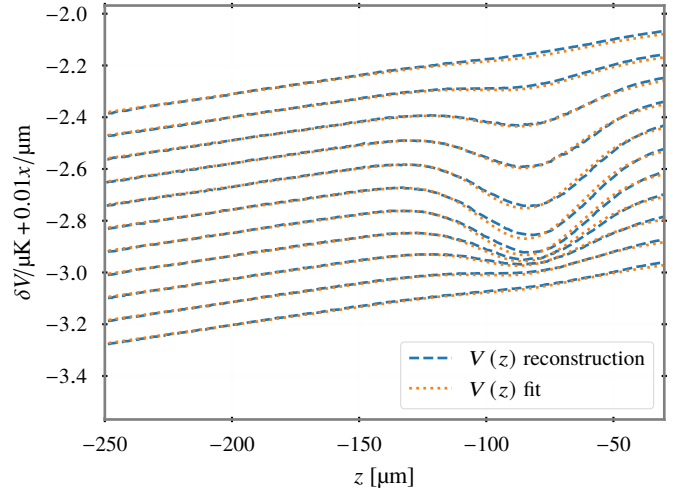


**Figure 9.** Comparison of the potential differences along the  $z$ -axis from phase reconstruction and fits for a number of fixed  $x$  positions. Each pair is matched at  $z = -200 \mu\text{m}$  to compensate for an overall offset in the phase reconstruction algorithm. Inconsistencies where the laser potential is stronger may be due to a small deviation from an ideal Gaussian potential shape, or from a breakdown of the impulse approximation.

\* [m.forbes@wsu.edu](mailto:m.forbes@wsu.edu)

† [engels@wsu.edu](mailto:engels@wsu.edu)

- [1] Shuming Yang and Guofeng Zhang. A review of interferometry for geometric measurement. *Measurement Science and Technology*, 29(10):102001, sep 2018.
- [2] B. P. Abbott et al. GW151226: Observation of Gravitational Waves from a 22-Solar-Mass Binary Black Hole Coalescence. *Phys. Rev. Lett.*, 116(24):241103, June 2016.
- [3] Kai Bongs, Michael Holynski, Jamie Vovrosh, Philippe Bouyer, Gabriel Condon, Ernst Rasel, Christian Schubert, Wolfgang P. Schleich, and Albert Roura. Taking atom interferometric quantum sensors from the laboratory to real-world applications. *Nature Reviews Physics*, 1(12):731–739, oct 2019.
- [4] N.P. Robins, P.A. Altin, J.E. Debs, and J.D. Close. Atom lasers: Production, properties and prospects for precision inertial measurement. *Physics Reports*, 529(3):265–296, aug 2013.
- [5] G. Rosi, F. Sorrentino, L. Cacciapuoti, M. Prevedelli, and G. M. Tino. Precision measurement of the Newtonian gravitational constant using cold atoms. *Nature*, 510(7506):518–521, jun 2014.
- [6] Chris Overstreet, Peter Asenbaum, Joseph Curti, Minjeong Kim, and Mark A. Kasevich. Observation of a gravitational Aharonov-Bohm effect. *Science*, 375(6577):226–229, January 2022.
- [7] A. D. Cronin, J. Schmiedmayer, and D. E. Pritchard. Optics and interferometry with atoms and molecules. *Rev. Mod. Phys.*, 81:1051–1129, 2009.
- [8] Sven Abend, Matthias Gersemann, Christian Schubert, Dennis Schlippert, Ernst M. Rasel, Matthias Zimmermann, Maxim A. Efremov, Albert Roura, Frank A. Narducci, and Wolfgang P. Schleich. Atom interferometry and its applications. In Ernst M. Rasel, Wolfgang P. Schleich, and Sabine Wölk, editors, *Foundations of Quantum Theory*, volume 197 of *Proceedings of the International School of Physics “Enrico Fermi”*, pages 345–392, Amsterdam, 2019. IOS Press.
- [9] Ben Stray, Andrew Lamb, Aisha Kaushik, Jamie Vovrosh, Anthony Rodgers, Jonathan Winch, Farzad Hayati, Daniel Boddice, Artur Stabrawa, Alexander Niggebaum, Mehdi Langlois, Yu-Hung Lien, Samuel Lellouch, Sanaz Roshanmanesh, Kevin Ridley, Geoffrey de Villiers, Gareth Brown, Trevor Cross, George Tuckwell, Asaad Faramarzi, Nicole Metje, Kai Bongs, and Michael Holynski. Quantum sensing for gravity cartography. *Nature*, 602(7898):590–594, feb 2022.
- [10] Stuart Moulder, Scott Beattie, Robert P. Smith, Naaman Tammuz, and Zoran Hadzibabic. Quantized supercurrent decay in an annular Bose-Einstein condensate. *Phys. Rev. A*, 86(1):013629, jul 2012.
- [11] L. Corman, L. Chomaz, T. Bienaimé, R. Desbuquois, C. Weitenberg, S. Nascimbène, J. Dalibard, and J. Beugnon. Quench-Induced Supercurrents in an Annular Bose Gas. *Phys. Rev. Lett.*, 113(13):135302, sep 2014.
- [12] S. Eckel, F. Jendrzejewski, A. Kumar, C. J. Lobb, and G. K. Campbell. Interferometric measurement of the current-phase relationship of a superfluid weak link. *Phys. Rev. X*, 4(3):031052, sep 2014.
- [13] G. Del Pace, K. Khani, A. Muzi Falconi, M. Fedrizzi, N. Grani, D. Hernandez Rajkov, M. Inguscio, F. Scazza, W. J. Kwon, and G. Roati. Imprinting persistent currents in tunable fermionic rings, 2022.
- [14] M.-O. Mewes, M. R. Andrews, D. M. Kurn, D. S. Durfee, C. G. Townsend, and W. Ketterle. Output Coupler for Bose-Einstein Condensed Atoms. *Phys. Rev. Lett.*, 78(4):582–585, 1997.
- [15] M. Naraschewski, A. Schenzle, and H. Wallis. Phase diffusion and the output properties of a cw atom-laser. *Phys. Rev. A*, 56(1):603, 1997.
- [16] W. Ketterle and H.-J. Miesner. Coherence properties of Bose-Einstein condensates and atom lasers. *Phys. Rev. A*, 56(4):3291–3293, 1997.
- [17] H. Steck, M. Naraschewski, and H. Wallis. Output of a pulsed atom laser. *Phys. Rev. Lett.*, 80(1):1–5, 1998.
- [18] I. Bloch, T. W. Hänsch, and T. Esslinger. Atom laser with a cw output coupler. *Phys. Rev. Lett.*, 82(15):3008–3011, 1999.
- [19] J. Schneider and A. Schenzle. Output from an atom laser: theory vs. experiment. *Appl. Phys. B*, 69(5–6):353–356, 1999.
- [20] R. J. Ballagh and C. M. Savage. The theory of atom lasers. *Mod. Phys. Lett.*, B14(suppo1):153–188, September 2000.
- [21] I. Bloch, T. W. Hänsch, and T. Esslinger. Measurement of the spatial coherence of a trapped Bose gas at the phase transition. *Nature*, 403(6766):166–170, 2000.
- [22] Y. Le Coq, J. H. Thywissen, S. A. Rangwala, F. Gerbier, S. Richard, G. Delannoy, P. Bouyer, and A. Aspect. Atom laser divergence. *Phys. Rev. Lett.*, 87(17):170403, 2001.
- [23] Immanuel Bloch, Michael Köhl, Markus Greiner, Theodor W. Hänsch, and Tilman Esslinger. Optics with an atom laser beam. *Phys. Rev. Lett.*, 87:030401, July 2001.
- [24] A. P. Chikkatur, Y. Shin, A. E. Leanhardt, D. Kielpinski, E. Tsikata, T. L. Gustavson, D. E. Pritchard, and W. Ketterle. A continuous source of Bose-Einstein condensed atoms. *Science*, 296(5576):2193–2195, 2002.
- [25] S. A. Haine, J. J. Hope, N. P. Robins, and C. M. Savage. Stability of continuously pumped atom lasers. *Phys. Rev. Lett.*, 88:170403, April 2002.
- [26] Geoffrey M. Lee, Simon A. Haine, Ashton S. Bradley, and Matthew J. Davis. Coherence and linewidth of a continuously pumped atom laser at finite temperature. *Phys. Rev. A*, 92:013605, July 2015.
- [27] Graeme Harvie, Adam Butcher, and Jon Goldwin. Coherence time of a cold-atom laser below threshold. *Optics Letters*, 45(19):5448, September 2020.
- [28] J.-F. Riou, Y. Le Coq, F. Impens, W. Guerin, C. J. Bordé, A. Aspect, and P. Bouyer. Theoretical tools for atom-laser-beam propagation. *Phys. Rev. A*, 77:033630, March 2008.
- [29] M. E. Mossman, T. M. Bersano, Michael McNeil Forbes, and P. Engels. Gravitational caustics in an atom laser. *Nature Comm.*, 12(1), December 2021.
- [30] Norman F. Ramsey. A molecular beam resonance method with separated oscillating fields. *Phys. Rev.*, 78(6):695–699, June 1950.
- [31] Brian H. Bransden and Charles Jean Joachain. *Physics of Atoms and Molecules*. Prentice Hall, Harlow, England ; New York, April 2003.
- [32] D Döring, J. E. Debs, N. P. Robins, C. Figl, P. A. Altin, and J. D. Close. Ramsey interferometry with an atom laser. *Optics Express*, 17(23):20661, oct 2009.
- [33] Gautam Ramola, Richard Winkelmann, Karthik Chandrashekhara, Wolfgang Alt, Peng Xu, Dieter Meschede, and Andrea Alberti. Ramsey imaging of optical traps. *Physical Review Applied*, 16(2), August 2021.
- [34] Stephen Taylor, Fan Yang, Brandon A. Freudenstein, and Benjamin Lev. A scanning quantum cryogenic atom microscope at 6K. *SciPost Physics*, 10(3), March 2021.
- [35] D. H. J. O’Dell. Quantum Catastrophes and Ergodicity in the Dynamics of Bosonic Josephson Junctions. *Phys. Rev. Lett.*, 109:150406, Oct 2012.
- [36] J. Mumford, W. Kirkby, and D. H. J. O’Dell. Catastrophes in non-equilibrium many-particle wave functions: universality and

- critical scaling. *J. Phys. B: At. Mol. Opt. Phys.*, 50:044005, 2017.
- [37] J. Mumford, E. Turner, D. W. L. Sprung, and D. H. J. O'Dell. Quantum spin dynamics in Fock space following quenches: Caustics and vortices. *Phys. Rev. Lett.*, 122:170402, May 2019.
- [38] Eric J. Heller, Ragnar Fleischmann, and Tobias Kramer. Branched flow. *Physics Today*, 74(12):44, December 2021.
- [39] J. H. Bruning, D. R. Herriott, J. E. Gallagher, D. P. Rosenfeld, A. D. White, and D. J. Brangaccio. Digital wavefront measuring interferometer for testing optical surfaces and lenses. *Appl. Opt.*, 13(11):2693–2703, Nov 1974.
- [40] Rigoberto Juarez-Salazar, Ceciibet Mendoza-Rodriguez, Jose E. Hernandez-Beltran, and Carlos Robledo-Sanchez. How do phase-shifting algorithms work? *European Journal of Physics*, 39(6):065302, oct 2018.
- [41] Jim Schwiegerling. *Optical Specification, Fabrication, and Testing*. SPIE—The International Society for Optical Engineering, 1st edition, October 2014.
- [42] Pierre Cartier and Cecile DeWitt-Morette. *Functional Integration: Action and Symmetries*. Cambridge Monographs on Mathematical Physics. Cambridge University Press, 2006.
- [43] T. A. Zapata and S. A. Fulling. WKB propagators in position and momentum space for a linear potential with a ‘ceiling’ boundary. *J. Phys. A*, 50(10):105303, February 2017.
- [44] W. van Dijk and M. Razavy. Exact and Glauber amplitudes in multi-channel scattering. *Can. J. Phys.*, 57(11):1952–1958, November 1979.
- [45] Robert G. Littlejohn and William G. Flynn. Geometric phases in the asymptotic theory of coupled wave equations. *Phys. Rev. A*, 44:5239–5256, October 1991.
- [46] C. Emmrich and H. Römer. Multicomponent WKB and quantization. *Acta Phys. Pol. B*, 27(10):2393, 1996.
- [47] K. Hagino and A. B. Balantekin. WKB approximation for multichannel barrier penetrability. *Phys. Rev. A*, 70:032106, September 2004.
- [48] B. Deissler, K. J. Hughes, J. H. T. Burke, and C. A. Sackett. Measurement of the ac Stark shift with a guided matter-wave interferometer. *Phys. Rev. A*, 77(3):031604, mar 2008.
- [49] Tobias Kramer and Mirta Rodríguez. Quantum theory of an atom laser originating from a Bose-Einstein condensate or a Fermi gas in the presence of gravity. *Phys. Rev. A*, 74:013611, July 2006. Erratum: [50].
- [50] Tobias Kramer and Mirta Rodríguez. Erratum: Quantum theory of an atom laser originating from a Bose-Einstein condensate or a Fermi gas in the presence of gravity. *Phys. Rev. A*, 75:069905, June 2007.
- [51] Kari Härkönen, Otto Vainio, and Kalle-Antti Suominen. Wavepacket analysis of interference patterns in output coupled atoms. *Phys. Rev. A*, 81:043638, April 2010.
- [52] C. Bracher, W. Becker, Gurvitz. S. A., M. Kleber, and M. S. Marinov. Three-dimensional tunneling in quantum ballistic motion. *Amer. J. Phys.*, 66(1):38–48, January 1998.
- [53] Olivier Vallée and Manuel Soares. *Airy Functions and Applications to Physics*. Imperial College Press, 2 edition, June 2010.
- [54] J. Schneider and A. Schenzle. Output from an atom laser: theory vs. experiment. *Applied Physics B*, 69(5):353–356, 1999.
- [55] Nicholas Robins, Craig Savage, and Elena A. Ostrovskaya. Atom-laser dynamics. *Phys. Rev. A*, 64:043605, September 2001.
- [56] Mark Edwards, David A. Griggs, Philip L. Holman, Charles W. Clark, S. L. Rolston, and W. D. Phillips. Properties of a Raman atom-laser output coupler. *J. Phys. B*, 32(12):2935–2950, January 1999.